

MS-IMAP - A Multi-Scale Graph Embedding Approach for Interpretable Manifold Learning

Shay Deutsch ^{*§}

shaydeu@gmail.com

Lionel Yelibi [§]

ylblio001@myuct.ac.za

Alex Tong Lin [§]

atlin271@gmail.com

Arjun Ravi Kannan [§]

arjun.kannan@gmail.com

June 6, 2024

1 Abstract

Deriving meaningful representations from complex, high-dimensional data in unsupervised settings is crucial across diverse machine learning applications. This paper introduces a framework for multi-scale graph network embedding based on spectral graph wavelets that employs a contrastive learning approach. A significant feature of the proposed embedding is its capacity to establish a correspondence between the embedding space and the input feature space which aids in deriving feature importance of the original features. We theoretically justify our approach and demonstrate that, in Paley-Wiener spaces on combinatorial graphs, the spectral graph wavelets operator offers greater flexibility and better control over smoothness properties compared to the Laplacian operator. We validate the effectiveness of our proposed graph embedding on a variety of public datasets through a range of downstream tasks, including clustering and unsupervised feature importance.

2 Introduction

Graph Embeddings and Manifold Learning [24, 1, 27, 28, 3] are pivotal in analyzing complex data structures prevalent in diverse machine learning applications. The emergent representations from these techniques offer insights into the underlying data structure in conjunction with downstream tasks like clustering and visualization and are particularly valuable when labels are unavailable or unreliable. However, limitations of these techniques include reliance on low frequencies of the graph Laplacian and k -Nearest Neighbors graph connectivity, which provide limited information, including in recent contrastive learning methods such as Uniform Manifold Approximation and Projection (UMAP). To address these limitations, this paper proposes three contributions. (1) A framework employing multi-scale graph representation using contrastive learning which enhances the expressiveness of an embedding by optimizing low and high-frequency information, capturing intricate data details. (2) A characterization of the theoretical properties of the representation

^{*}Corresponding author.

[§]Emerging Capabilities Research Group, Discover Financial Services Inc., Riverwoods, IL.

power of the spectral graph wavelets (SGW) operator by considering functions sampled from the Paley-Wiener spaces [22] on combinatorial graphs and a demonstration of the flexibility and better control over smoothness properties of the SGW operator in comparison to the Laplacian operator. (3) A novel sampling technique that leverages the graph structure by sampling edges or nodes from a distribution reflecting network characteristics.

A key distinction between our approach and many manifold learning methods such as UMAP is that we leverage multi-scale graph representation (using SGW) to increase the dimensionality of the data thus enhancing data representation learning. On the other hand, other manifold learning techniques predominantly employ nonlinear dimensionality reduction to reduce the dimensions of the output embedding space. We use stochastic gradient descent (SGD) to optimize the embedding space and employ a novel contrastive learning approach using a 3D-tensor to capture both low and high frequencies.

Another limitation of non-linear manifold learning methods is they inherently lack direct connections to input features, thereby limiting their ability to offer interpretable results which is crucial in various applications (e.g. in finance where customer behavior needs to be summarized with a few important features to design products or strategies benefiting them and in biology where easily interpretable features may lead to life saving discoveries). Although not the main focus of this article, our proposed approach establishes a mapping between the original features and the constructed optimized embeddings and enables the measurement of the importance of the original features with respect to the embedding space (see Figure.1 for an illustration of the mapping generated by the proposed embedding). To the best of our knowledge, current manifold learning techniques produce embeddings lacking explicit interpretation. In contrast, our approach demonstrates the ability to generate interpretable embedding representations, while also being competitive with the state-of-the-art graph embeddings across applications such as finance, vision, and biology.

3 Related Work

Extensive efforts have been dedicated to exploring non-linear dimensionality reduction aimed at achieving a low-dimensional embedding that preserves the underlying manifold structure. Early manifold learning techniques include Locally Linear Embedding (LLE) [24], Laplacian Eigenmaps [1], Isomap [27], Diffusion Maps [2], and t-distributed Stochastic Neighbor Embedding (t-SNE) [28].

Balancing local and global structure in the resulting embeddings is challenging in the presence of noise. To address the challenge, researchers have introduced de-noising methods [17, 10, 6, 9, 5, 11, 7, 8]. These techniques seek to enhance algorithms robustness, thereby broadening the applicability of these techniques in real-world scenarios.

UMAP [21] has proven effective in providing vivid visualizations and cluster separation, yet its reliance on Laplacian Eigenmaps initialization and negative sampling optimization has limitations. Laplacian Eigenmaps initialization focuses on low-frequency signal overlooking higher-frequency patterns. It uniformly samples edges without considering topological importance, overemphasizing graph connectivity and introducing further distortion.

Recent work [4] further highlights that negative sampling has a significant impact on the effective loss and introduces distortions with t-SNE and UMAP which motivates the exploration of alternate sampling schemes. Other relevant studies include [30] which investigates competing negative sampling strategies, [25] on generalization error bounds, and [20] on topological and sampling bias due to high degree nodes.

The lack of explicit mapping linking the original high dimensional dataset to its low dimensional embedding has prevented their use in areas where interpretability is critical. Establishing this link clearly would lead to a better understanding of the original feature space and improve feature selection, understanding of

the resulting visualizations, and robustness to noise [18, 13, 31].

SGW serve as an efficient tool for localization in both the spectral and vertex domains, playing a crucial role in our method (see Section 5.1 for details). SGW are constructed by applying a set of bandpass filters to the eigenvalues of the graph Laplacian, enabling multi-resolution representation of graph signals. An alternative multi-scale framework for analyzing functions on graphs is Diffusion Wavelets [23]. The Geometric Graph Scattering transform and the Graph Scattering Transform [14] utilize Diffusion Wavelets to extract graph features, which are then employed in graph classification tasks. In our work, we leverage the localization properties of SGW to develop a novel feature representation scheme, achieving superior performance in our target applications.

4 Preliminaries

Consider a set of points $\mathbf{x} = \{\mathbf{x}_i\}, i = 1, \dots, N, \mathbf{x}_i \in \mathbb{R}^D$, which are sampled from an unknown manifold $M \subset \mathbb{R}^D$. An undirected, weighted graph $G = (V, \mathbf{W})$, is constructed over \mathbf{x} , where V corresponds to the nodes and \mathbf{W} to the set of edges on the graph. The adjacency matrix $\mathbf{W} = (w_{ij})$ consists of the weights w_{ij} between node i and node j . The weights can be chosen using different techniques, such as the Gaussian kernel function or adaptive graph construction. If the weights are chosen using the Gaussian kernel function then

$$(\mathbf{W})_{ij} = \begin{cases} \exp\left(\frac{-\|\mathbf{x}_i - \mathbf{x}_j\|_2^2}{2\sigma_D^2}\right) & \text{if } \mathbf{x}_j \in \text{kNN}(\mathbf{x}_i) \\ 0 & \text{otherwise} \end{cases} \quad (1)$$

where $\|\cdot\|$ denotes the L2 distance between the points $\mathbf{x}_i, \mathbf{x}_j$, $\text{kNN}(\mathbf{x}_i)$ denotes the k nearest neighbors of \mathbf{x}_i , and $2\sigma_D^2$ are parameters used to construct the graph.

An alternative is to use adaptive graph construction as proposed in [21]. The global smoothness of the graph signal function $f \in \mathbb{R}^N$ (a function over the vertices of the graph G) is defined using the graph Laplacian quadratic form as follows: $\|\nabla f\|^2 = \sum_{V(i,j)} w_{ij} (f(i) - f(j))^2 = f^T \mathbf{L} f$, where \mathbf{L} denotes the combinatorial graph Laplacian, defined as $\mathbf{L} = \mathbf{D} - \mathbf{W}$, with \mathbf{D} the diagonal degree matrix with entries $d_{ii} = d(i)$. The degree $d(i)$ of vertex i is defined as the sum of weights of edges that are connected to i . The normalized Laplacian is defined as $\mathbf{L}_N = \mathbf{D}^{-\frac{1}{2}} \mathbf{L} \mathbf{D}^{-\frac{1}{2}} = \mathbf{I} - \mathbf{D}^{-\frac{1}{2}} \mathbf{W} \mathbf{D}^{-\frac{1}{2}}$ and its real eigenvalues are in the interval $[0, 2]$. The eigenvalues and eigenvectors of \mathbf{L} are $\lambda_1, \dots, \lambda_N$ and ϕ_1, \dots, ϕ_N , respectively. The graph Fourier transform (GFT) \hat{f} of the graph signal f is defined as the expansion of f in terms of the eigenvectors ϕ of the graph Laplacian, so that for frequency λ_l we have:

$$\hat{f}(\lambda_l) = \sum_i f(i) \phi_l^*(i). \quad (2)$$

We will denote the matrix representations of the eigenvectors and eigenvalues of the graph Laplacian \mathbf{L} as Φ, λ , respectively. Our approach assumes that all graph signals $f_r \in \mathbb{R}^N$ used to create the embedding correspond to the input coordinates, $\mathbf{x} = (f_1, f_2, \dots, f_r, \dots, f_D)$. The output embedding space provides a multi-scale representation approximating the intrinsic manifold coordinates.

4.1 Multi-scale representations using SGW

In the last two decades, several multi-scale representations using irregular graphs have been suggested, including SGW [15] and Diffusion Wavelets [23]. In this work we focus on the multi-scale graph transform utilizing SGW. SGW provides a natural way of trading off between spectral and spatial resolution, since

the SGW coefficients are localized in both domains. These wavelets are constructed using a kernel function $g(\mathbf{L})$ operator, which acts on a function by modulating each of its Fourier modes [15], that helps in capturing a trade off between vertex (spatial) and spectral localization. Spatial localization in the graph domain is implicitly controlled by a single wavelet scale parameter defined in the spectral domain, such that the more the vertex is localized in the vertex domain, the spectral band is wider. The scale parameter enables the model to adjust the effective neighborhood sizes to the properties of the data.

To represent a signal $f \in \mathbb{R}^N$ in multiple scales $S = [s_1, s_2, \dots, s_K]$, the SGW transform is constructed as follows: Assume that $g(\lambda)$ is a filter in the spectral domain. Let $\delta_i \in \mathbb{R}^N$ be the delta function centred at the vertex $i \in G : \delta_i(j) = 1$ if $i = j$, and $\delta_i(j) = 0$ otherwise. Given a bandpass filter $g(\lambda)$ and a wavelet centered on node i at scale s , the wavelets $\psi(s, i)$, $i = 1, \dots, N$ are calculated by applying them to the delta function on a single vertex i , given by

$$\psi(s, i) = \Phi g(s\lambda) \Phi^T \delta_i \quad (3)$$

The value of $\psi(s, i)$ with respect to a vertex m can be written as $\psi(s, i)(m) = \sum_{l=1}^N g(s\lambda_l) \phi_l^*(i) \phi_l(m)$. Given a graph signal $f \in \mathbb{R}^N$, the **SGW coefficient** at node i and scale s can be expressed as follows:

$$\psi_f(s, i) = \sum_{l=1}^N g(s\lambda_l) \hat{f}(\lambda_l) \phi_l(i) \quad (4)$$

Fast computation using Chebyshev polynomials: Directly computing the SGW coefficients requires calculating the entire eigensystem of the Laplacian, which is computationally intensive - $O(N^3)$ for N points. Instead, Hammond et al. [15] suggested computing the SGW using a fast algorithm based on approximating the scaled generating kernels through low-order polynomials of \mathbf{L} applied to the input data (details in Appendix).

5 Our Proposed framework: Multi-scale IMAP

In this section, we introduce Multi-scale IMAP, a framework for interpretable embedding via manifold learning utilizing a multi-scale graph representation. This approach enables us to maintain global regularity and preserve local structure without sacrificing interpretability. Our method imposes a differentiable structure on the mapping $h : \mathbf{x} \rightarrow \psi_{\mathbf{x}}$, supported on a discrete graph $G = (V, \mathbf{W})$, where $\psi_{\mathbf{x}}$ represents the encoded multi-scale graph transform of \mathbf{x} . Multi-scale IMAP consists of three main components:

Step 1: Features representation encoding using multi-scale graph representation.

In this step, our approach constructs a multi-scale graph representation by incorporating feature signals through the SGW Transform across multiple scales and graph frequencies. We introduce two methods for encoding multi-scale transform: in the first, based on simple concatenation, all of the features transformed for all scales are represented by concatenating all the SGW coefficients for each point in a vector form. In the second based on 3D tensor optimization, we construct a 3D tensor with dimensions $K \times N \times D$. We leverage the encoded 3D tensor structure to align the optimized embedding with all scales simultaneously to enforce differentiable structure of the transformed features.

Step 2: Optimization design using multi-scale network structure.

We integrate the multi-scale representation within the SGD optimization framework, simultaneously leveraging both low and high-frequency information. This integration leads to fine-grained manifold regularization and improved robustness in downstream tasks.

Step 3: Network features sampling strategy.

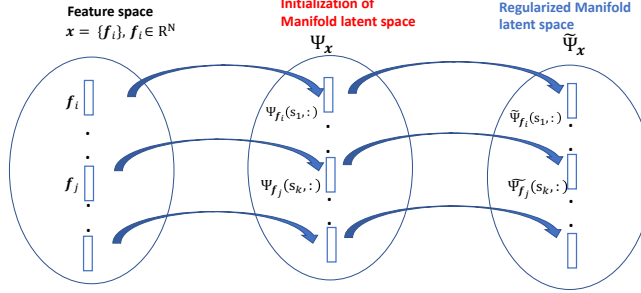


Figure 1: The encoding step of our framework is illustrated as a mapping between each coordinate of the input features and a corresponding dimension in the embedding space. This mapping is facilitated through our proposed approach, which aligns the input dimensions of the features with the latent embedding space. By establishing this correspondence, we acquire the capability to interpret each dimension in the embedding space. Such interpretation allows for various analyses, including providing feature importance relative to the latent space.

Our approach introduces a sampling scheme that selects network features based on their estimated importance in the graph network. Employed within the optimization using SGD, this adaptive strategy dynamically prioritizes and focuses on informative parts of the graph during the embedding process. This adaptability enhances the optimization process, leading to increased efficiency in generating embeddings.

5.1 Feature Representation to encode multi-scale structure in the optimized embeddings

We propose two alternative methods to encode multi-scale representations used for subsequent optimization. Note that for both method 1 and method 2, each dimension in the embedding space is constructed using a single feature in the original feature set, which is an essential characteristic that can be leveraged for interpreting graph embeddings.

(i) **Encoding Method 1:** The first encoding method involves concatenating the multi-scale representation of all features and filters (associated with different scales) into a single vector representation for each point. This results in a matrix representation denoted as ψ_x . Note that we designate the concatenation using \parallel , with

$$c(\psi_{f_i}(s_k, :), \psi_{f_j}(s_k, :)) = \psi_{f_i}(s_k, :) \parallel \psi_{f_j}(s_k, :)$$

denoting the concatenation of the vectors corresponding to the multi-scale representation $\psi_{f_i}(s_k, :)$ and $\psi_{f_j}(s_k, :)$. For method (i) (also noted as method 1) where all features and all scales are concatenated together, the resulting matrix ψ_x can be represented as

$$\psi_x = \psi_{f_1}(s_1, :) \parallel \psi_{f_2}(s_1, :) \parallel \dots \parallel \psi_{f_{D-1}}(s_K, :) \parallel \psi_{f_D}(s_K, :)$$

where $\psi_x \in \mathbb{R}^{KD} \times \mathbb{R}^N$.

Algorithm 1: Encoding multi-scale structure in the optimized embeddings

Input: Set of points $\{\mathbf{x}_i\}_{i=1}^N$.
Output: Initial Node Embeddings $\psi_{\mathbf{x}}$.
Step 1: Construct $G = (V, \mathbf{W})$ from $\{\mathbf{x}_i\}_{i=1}^N$.
Step 2: Construct the Laplacian \mathbf{L} .
Step 3: Compute $\lambda_{\max}(\mathbf{L})$.
Step 4: Initial Embedding construction:
For $r = 1, \dots, D$ associated with the feature signals $\{f_r\}$ do:
Compute $\psi_{f_r}(s_j, :)$ at scales $s_j, j = 1, \dots, K$ using Chebyshev approximation.
If Encoding Method 1: Concatenate $\psi_{f_r}(s_j, :), j = 1, \dots, K, r = 1, \dots, D$ in a matrix form $\psi_{\mathbf{x}} \in \mathbb{R}^{KD} \times \mathbb{R}^N$.
If Encoding Method 2: Concatenate $\psi_{f_r}(s_j, :)$ for $r = 1, \dots, D$ in a matrix form $\psi_{\mathbf{x}}(s_j, :, :)$ for each fixed scale s_j , representing all scales using 3D tensor $\psi_{\mathbf{x}} \in \mathbb{R}^K \times \mathbb{R}^D \times \mathbb{R}^N$.

(ii) **3D-Tensor Encoding - Method 2** The second encoding method concatenates the multi-scale representation for all features at a fixed scale, generating a matrix representation $\psi_{\mathbf{x}}(s_j, :, :) \in \mathbb{R}^D \times \mathbb{R}^N$ for each scale s_j . For method 2, after concatenating all f_i at a fixed scale s_j , we have

$$\psi_{\mathbf{x}}(s_j, :, :) = \psi_{f_1}(s_j, :) \| \psi_{f_2}(s_j, :) \| \dots \| \psi_{f_D}(s_j, :)$$

The optimization can be performed separately for each scale s_j , or jointly for all scales s_j using the 3D tensor $\psi_{\mathbf{x}} \in \mathbb{R}^K \times \mathbb{R}^D \times \mathbb{R}^N$. We detail the proposed feature representation encoding methods in the pseudo code algorithm 1.

5.2 Optimization

We propose to use optimization based on SGD that begins with the initial embedding within the spectral graph domain. While employing positive and negative sampling, our aim is to optimize the embedding space directly in the SGW domain, revealing the intrinsic structure of manifold data while retaining high-frequency information associated with the graph Laplacian. This optimization within the SGW domain provides more effective regularization, allowing for the direct removal of noise from each spectral band. We outline the steps of the proposed approach, presenting several alternatives for optimization through the incorporation of multi-scale representations (refer to method 1 and method 2 in the algorithm description below).

1. Optimize Embedding Method 1:

Given the encoded multi-scale representation $\psi_{\mathbf{x}} \in \mathbb{R}^{KD} \times \mathbb{R}^N$ perform optimization in the SGW domain, using the following fuzzy cross entropy loss function:

$$\mathcal{L}(\tilde{\psi}_{\mathbf{x}} | \mathbf{W}) = \sum_{i,j} \left(w_{ij} \log \frac{w_{ij}}{v_{ij}^{\psi_{\mathbf{x}}}} + (1 - w_{ij}) \log \frac{1 - w_{ij}}{1 - v_{ij}^{\psi_{\mathbf{x}}}} \right) \quad (5)$$

$$\text{where } v_{ij}^{\psi_{\mathbf{x}}} = \frac{1}{1 + \|\psi_{\mathbf{x}_i} - \psi_{\mathbf{x}_j}\|^2}.$$

Dropping terms that do not depends on $\psi_{\mathbf{x}_i}$, the gradient of the loss is approximated by:

$$\frac{\partial \mathcal{L}(\tilde{\psi}_{\mathbf{x}} | \mathbf{W})}{\partial \psi_{\mathbf{x}_i}} \sim \sum_j w_{ij} v_{ij}^{\psi_{\mathbf{x}}} (\psi_{\mathbf{x}_i} - \psi_{\mathbf{x}_j}) - \sum_j \frac{1}{\|\psi_{\mathbf{x}_i} - \psi_{\mathbf{x}_j}\|^2} v_{ij}^{\psi_{\mathbf{x}}} (\psi_{\mathbf{x}_i} - \psi_{\mathbf{x}_j}) \quad (6)$$

Our optimization process involves using SGD with positive and negative sampling, similar to recent graph embeddings method such as UMAP and LargeVis [26]. Positive edge samples are associated with attraction (first term on the right hand side), while negative samples (second term on the right hand side) refer to a pair of nodes that are not connected in the graph, which create repulsion among dissimilar points.

Output: Regularized embedding space $\tilde{\psi}_{\mathbf{x}}$.

2. 3D-Tensor Based Optimization: Embedding Method 2:

In method 2, the encoded manifold representation given is a 3D tensor $\psi_{\mathbf{x}} \in \mathbb{R}^K \times \mathbb{R}^D \times \mathbb{R}^N$. A SGD update rule at iteration t applied to the 3D tensor is:

$$(\tilde{\psi}_{\mathbf{x}}^{(t+1)})_{i,j,k} = (\tilde{\psi}_{\mathbf{x}}^{(t)})_{i,j,k} - \alpha \frac{\partial \mathcal{L}}{\partial \psi_{\mathbf{x}}}_{i,j,k} \quad (7)$$

where α is the learning parameter. In our case we employ the cross entropy loss function:

$$\mathcal{L}(\tilde{\psi}_{\mathbf{x}} | \mathbf{W}) = \sum_{i,j,k} \left(w_{ij} \log \frac{w_{ij}}{v_{ij}^{\psi_{\mathbf{x}}(s_k, :, :)}} + (1 - w_{ij}) \log \frac{1 - w_{ij}}{1 - v_{ij}^{\psi_{\mathbf{x}}(s_k, :, :)}} \right) \quad (8)$$

We apply the optimization based on SGD with respect to each scale s_k :

$$\mathcal{L}(\tilde{\psi}_{\mathbf{x}}(s_k, :, :) | \mathbf{W}) = \sum_{i,j} \left(w_{ij} \log \frac{w_{ij}}{v_{ij}^{\psi_{\mathbf{x}}(s_k, :, :)}} + (1 - w_{ij}) \log \frac{1 - w_{ij}}{1 - v_{ij}^{\psi_{\mathbf{x}}(s_k, :, :)}} \right) \quad (9)$$

which has the gradient of the loss is approximated by:

$$\begin{aligned} \frac{\partial \mathcal{L}(\tilde{\psi}_{\mathbf{x}}(s_k, :, :) | \mathbf{W})}{\partial \psi_{\mathbf{x}_i}(s_k, :, :)} &= \sum_j w_{ij} v_{ij}^{\psi_{\mathbf{x}}(s_k, :, :)} (\psi_{\mathbf{x}_i}(s_k, :, :) - \psi_{\mathbf{x}_j}(s_k, :, :)) \\ &- \sum_j \frac{1}{\|\psi_{\mathbf{x}_i}(s_k, :, :) - \psi_{\mathbf{x}_j}(s_k, :, :)\|^2} v_{ij}^{\psi_{\mathbf{x}}(s_k, :, :)} (\psi_{\mathbf{x}_i}(s_k, :, :) - \psi_{\mathbf{x}_j}(s_k, :, :)) \end{aligned}$$

The optimization process uses SGD with positive and negative sampling for all scales s_k given a pair of positive or negative pair of nodes i, j .

We compute the final embedding by summing up all the optimized embeddings with respect to each scale s_k

$$\tilde{\psi}_{\mathbf{x}} = \sum_k \tilde{\psi}_{\mathbf{x}}(s_k, :, :) \quad (10)$$

In the 3D tensor based optimization method 2, the dimensionality of the final embedding $\tilde{\psi}_{\mathbf{x}} \in \mathbb{R}^D \times \mathbb{R}^N$, maintaining the same dimensionality as the original input, and thus there exists a one-to-one correspondence between the coordinates of the input features \mathbf{x} and $\tilde{\psi}_{\mathbf{x}}$. This correspondence ensures that each dimension of the feature space is directly mapped to a single dimension in the embedding space $\tilde{\psi}_{\mathbf{x}}$.

Sampling approaches from network features: We propose a strategic sampling of edges, which further refines the optimization by assessing the significance of edges with respect to the topological structure of the graph. Specifically, we construct probability distribution over V (or \mathbf{W}), providing the significance of each node/edge, and sample from this distribution. We also propose a novel method to implement the sampling strategy, rather than selecting edges randomly as in [21, 26]. Refer to Appendix for more details.

6 Theoretical results: Sampling set for Smooth Manifolds with functions defined over Paley-Wiener Spaces

In this section, we characterize the theoretical properties of the representation power of the SGW operator by considering functions sampled from the Paley-Wiener spaces [22] on combinatorial graphs. Pesenson introduced the Paley-Wiener spaces and demonstrated that Paley-Wiener functions of low type are uniquely determined by their values on certain subsets, known as uniqueness sets U . We show that the SGW operator can represent functions f within the Paley-Wiener space more efficiently than the graph Laplacian operator \mathcal{L} . This efficiency is demonstrated by showing that the SGW operator is more effective in representing functions with larger bandwidth ω in the Paley-Wiener spaces (i.e., with higher frequencies) using subsets of nodes from the uniqueness sets U .

To characterize the representation properties of functions defined over $PW_\omega(G)$, we employ the notion of the Λ -set, introduced by Pesenson which is central to our investigation. Formally, the Paley-Wiener space of ω -bandlimited signals is defined as $PW_\omega(G) = \{f \mid \hat{f}(\lambda) = 0 \forall \lambda > \omega\}$. The space $L_2(G)$ is defined as the Hilbert space of all complex-valued functions, and $L_2(S)$ is defined as the space of all functions from $L_2(G)$ with support in S : $L_2(S) = \{\varphi \in L_2(G) \mid \varphi(v) = 0, v \in V(G) \setminus S\}$.

The Λ -set is defined as follows: a set of vertices $S \subset V$ is a $\Lambda(S)$ -set if any $\varphi \in L_2(S)$ satisfies the inequality $\|\varphi\| \leq \Lambda \|\mathcal{L}\varphi\|$ for some constant $\Lambda(S) > 0$. The infimum of all $\Lambda > 0$ for which S is a Λ -set is denoted by Λ .

The ability of the SGW operator to efficiently represent functions $f \in PW_\omega(G)$ can be summarized in the following theorem, which highlights the role of the Λ_ψ -set with respect to the operator ψ . We show that any signal $f \in PW_\omega(G)$, where $\lambda_1 \leq \omega < \Omega_G$ for some $\Omega_G < \lambda_N$, can be uniquely represented by its samples on the uniqueness set U using the SGW operator. Under certain conditions related to the SGW operator, its associated Λ_ψ -set is smaller than the Λ -set associated with the Laplacian operator.

Theorem 1 *Let $G = (V, \mathbf{W})$ be a connected graph with n vertices and $f \in PW_\omega(G)$ for $\lambda_1 \leq \omega < \lambda_{\max}$. The SGW operator ψ can be constructed such that the set S is a Λ_ψ -set and the set $U = V \setminus S$ is a uniqueness set for any space $PW_\omega(G)$ with $\omega < 1/\Lambda_\psi$ and $\Lambda_\psi < \Lambda$ for any $\varphi \in L_2(S)$, where Λ is the Λ -set of the Laplacian operator.*

The proof is provided in the Appendix.

7 Experimental Results

We demonstrate the advantage of our approach over existing approaches using both synthetic and real datasets. We evaluate our method by testing its clustering performance using the output embedding and comparing it to several representative methods, including UMAP, t-SNE, Diffusion Maps, ISOMAP, and HeatGeo [19]. For HeatGeo, we hyperparameter tune the performance on each dataset and report the best one in Section 11. For each dataset, we briefly describe their properties and leave fuller details in Section 9.

Evaluation metrics: We test performance using the Adjusted Rand Index (ARI) and Adjusted Mutual Information (AMI). In all experiments we used k -means to cluster the data in the embedding space.

7.1 Synthetic dataset

We assess the robustness of our method using the two moons dataset, which is a 2D manifold depicting two interleaving half-circles. We sampled $N = 600$ points, and set the Gaussian noise's standard deviation to

0.12. While spectral based methods such as UMAP are effective under relatively “modest” noise levels, their performance deteriorates significantly in the presence of larger amounts of noise (See Figure 3). As shown in Table 1, our approach shows robustness to noise and correctly clusters most points in two moons manifold, despite the large amount of noise, and outperforms competing methods. We do further experiments on more synthetic datasets in Section 10.

Method / Accuracy	ARI	AMI
UMAP	0.54	0.51
t-SNE	0.42	0.35
ISOMAP	0.36	0.3
Diffusion Maps	0.25	0.19
HeatGeo	0.54	0.52
MS-IMAP Method 1	0.75	0.73
MS-IMAP Method 2	0.89	0.87

Table 1: Comparison of clustering performance on the Two Moons datasets.

7.2 Real Datasets

We study the performance of MS-IMAP compared to other methods for real datasets. We chose a mix of financial, biological, and image datasets: the Census dataset [12] is a financial dataset containing information about individuals extracted from the 1994 US Census; the Zilionis dataset [32] is a biological dataset containing single-cell sequencing data from different types of cells, and the Animals with Attributes (AWA) [29] dataset is an image dataset containing images of animals. More information about each dataset can be found in Section 9.

As shown in Table 2, MS-IMAP Method 2 obtains the best performance across all datasets, with a tie between UMAP and MS-IMAP Method 2 in the AWA dataset. In the Census dataset, MS-IMAP Method 2 achieves a 47% increase in ARI over HeatGeo, the next best method excluding our own. In the Zilionis dataset, MS-IMAP 2 achieves a 9% increase in ARI over t-SNE (we found issues running the official HeatGeo code [19] on Zilionis, so were unable to obtain results for this dataset). And in AWA, we have the ARI of MS-IMAP Method 2 is slightly better than UMAP.

Dataset	Census		Zilionis		AWA	
	Method / Accuracy	ARI	AMI	ARI	AMI	ARI
UMAP	0.05	0.08	0.45	0.71	0.73	0.80
t-SNE	0.01	0.02	0.64	0.34	0.68	0.76
HeatGeo	0.15	0.10	N/A	N/A	0.65	0.74
MS-IMAP Method 1	0.15	0.14	0.69	0.76	0.72	0.80
MS-IMAP Method 2	0.22	0.15	0.70	0.76	0.74	0.81

Table 2: Clustering results comparison using ARI and AMI the Census, Zilionis, and AWA datasets. Note HeatGeo had code execution issues on the Zilionis dataset.

8 Explicit Feature Correspondence with Laplacian Scoring

The correspondence established between the features and the embedding space becomes valuable in obtaining feature importance. One simple measure for feature importance is the Laplacian score (LS) [16], which evaluates each feature based on its correlation with the graph Laplacian eigensystem. Specifically, the importance of a feature $f_r \in \mathbb{R}^N$ is determined from the importance of its corresponding coordinate l in the embedding space, $\tilde{\psi}_{x_l}$. We calculate the Laplacian score [16] with respect to the embedding features $\tilde{\psi}_x$ using its graph Laplacian \mathbf{L} and its associated degree matrix \mathbf{D} . This is achieved by first removing the mean and then computing the Laplacian score using:

$$L_s(\tilde{\psi}_x)_l = \frac{(\tilde{\psi}_x)_l^T \mathbf{L} (\tilde{\psi}_x)_l}{(\tilde{\psi}_x)_l^T \mathbf{D} (\tilde{\psi}_x)_l} \quad (11)$$

Smaller scores imply that the feature $(\tilde{\psi}_x)_l$ has a larger projection on the subspace of the eigenvectors associated with the smallest eigenvalues, indicating higher importance with respect to the graph structure. Each coordinate l in the embedding space $\tilde{\psi}_x$, namely $(\tilde{\psi}_x)_l$, was constructed using a single coordinate of the original feature f_r space. Hence, the feature importance of $(\tilde{\psi}_x)_l$ can be explicitly interpreted as the importance of the associated original feature.

8.1 Application to Feature importance

We demonstrate the effectiveness of our approach using a computer vision example where providing interpretation, including feature importance, is of significant interest. Here we show in Figure (2) the estimated Laplacian score of the 85 semantic attributes for the AWA datasets sorted from high to low. Because the Laplacian score is a function of explained variance, one can argue that this score is a measure of feature information and we observe that the number of features capturing the highest scores is small (on the order of 10). This result highlights that most of the information in the data-set which correlates with the embedding is captured by a small group of variables which suggests their relatively higher importance. The Laplacian score ranking allows us to select a small number of variables for further analysis in order to better understand the output of statistical studies performed using the embedded data.

8.2 Runtime and Computational Complexity

The execution time of our method with Python code implementation with 32 cores Intel Xeon 8259CL running at 2.50Ghz and 256GB of RAM on the Cancer QC data-set of 48,969 samples and 306 features took 12.44 mins using Method 1. The computational complexity of Multi-Scale IMAP is of $O(ND \log(N))$. Additional details are provided in the appendix.

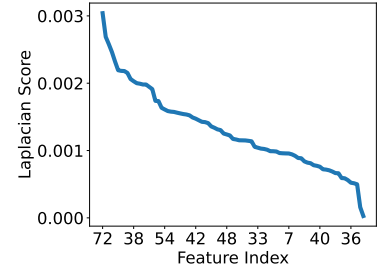


Figure 2: AWA Dataset Laplacian Score plotline showing in order from high to low, the importance of the original features with respect to the embeddings.

8.3 Conclusions and Limitations

Identifying the key drivers of high-dimensional datasets is a necessary ingredient to take advantage of unlabelled data in many practical applications in fields such as finance and biology. In this article, we introduce a novel contrastive learning framework for manifold learning via graph embeddings, capitalizing on both low and high-frequency information. In particular, we use SGW to construct a multi-scale graph representation of the underlying input feature space. We then use an SGD-based optimization scheme together with innovative strategies such as 3D Tensor encoding to derive the embeddings. We study the theoretical properties of the spectral graph wavelet (SGW) representation by considering functions in Paley-Wiener spaces on combinatorial graphs and prove that the SGW operator provides a more effective representation using the concept of the Λ -set. Finally, we show that the embeddings are interpretable using a simple derivation of feature importance of the embedding and original feature spaces. The construction of our methodology for generating the embeddings implicitly gives us a way to tie the original and transformed feature spaces together which is lacking in current non-linear manifold learning techniques to the best of our knowledge.

Limitations: While our work has demonstrated several significant properties with strong performance on challenging datasets, it is not without limitations. Firstly, we rely on the assumption that the features, and thus the similarity measure, adequately capture information to reveal geodesic distances between manifold points. Secondly, utilizing the current optimization framework with SGD may present difficulties when extending to out-of-sample problems. Furthermore, although our embedding feature correspondence proves valuable in assessing feature importance through a global method, there remains potential for enhancement through the incorporation of local methods.

References

- [1] Mikhail Belkin and Partha Niyogi. Laplacian eigenmaps for dimensionality reduction and data representation. *Neural Computation*, 2003.
- [2] R. R. Coifman, S. Lafon, A. B. Lee, M. Maggioni, B. Nadler, F. Warner, and S. W. Zucker. Geometric diffusions as a tool for harmonic analysis and structure definition of data: Diffusion maps. *Proceedings of the National Academy of Sciences of the United States of America*, 2005.
- [3] R. R. Coifman, S. Lafon, A. B. Lee, M. Maggioni, F. Warner, and S. Zucker. Geometric diffusions as a tool for harmonic analysis and structure definition of data: Diffusion maps. In *Proceedings of the National Academy of Sciences*, 2005.
- [4] Sebastian Damrich and Fred A. Hamprecht. On umap’s true loss function. In *Neural Information Processing Systems*, 2021.
- [5] Shay Deutsch, Andrea L. Bertozzi, and Stefano Soatto. Zero shot learning with the isoperimetric loss. In *AAAI 2020*.
- [6] Shay Deutsch, Soheil Kolouri, Kyungnam Kim, Yuri Owechko, and Stefano Soatto. Zero shot learning via multi-scale manifold regularization. *CVPR*, 2017.
- [7] Shay Deutsch and Gerard Medioni. Intersecting manifolds: Detection, segmentation, and labeling. In *Proceedings of the Twenty-Fourth International Joint Conference on Artificial Intelligence*, 2015.
- [8] Shay Deutsch and Gerard Medioni. Unsupervised learning using the tensor voting graph. In *Scale Space and Variational Methods in Computer Vision (SSVM)*, 2015.

- [9] Shay Deutsch and Gérard G. Medioni. Learning the geometric structure of manifolds with singularities using the tensor voting graph. *Journal of Mathematical Imaging and Vision*, 57(3):402–422, 2017.
- [10] Shay Deutsch, Antonio Ortega, and Gerard Medioni. Manifold denoising based on spectral graph wavelets. *International Conference on Acoustics, Speech and Signal Processing (ICASSP)*, 2016.
- [11] Shay Deutsch, Antonio Ortega, and Gérard G. Medioni. Robust denoising of piece-wise smooth manifolds. In *2018 IEEE International Conference on Acoustics, Speech and Signal Processing, ICASSP 2018, Calgary, AB, Canada, April 15-20, 2018*, pages 2786–2790, 2018.
- [12] Dheeru Dua and Casey Graff. Uci machine learning repository. *2017 IEEE Conference on Computer Vision and Pattern Recognition (CVPR)*, 2017.
- [13] Christopher Frye, Damien de Mijolla, Tom Begley, Laurence Cowton, Megan Stanley, and Ilya Feige. Shapley explainability on the data manifold. In *International Conference on Learning Representations*, 2021.
- [14] Fernando Gama, Joan Bruna, and Alejandro Ribeiro. Stability of graph scattering transforms. *Proceedings of the 33rd International Conference on Neural Information Processing Systems*, 2019.
- [15] David K. Hammond, Pierre Vandergheynst, and Rémi Gribonval. Wavelets on graphs via spectral graph theory. *Applied and Computational Harmonic Analysis*, 2011.
- [16] Xiaofei He, Deng Cai, and Partha Niyogi. Laplacian score for feature selection. In *NIPS*, pages 507–514, 2005.
- [17] Matthias Hein and Markus Maier. Manifold denoising. In *Advances in Neural Information Processing Systems*, 2006.
- [18] Babak Hosseini and Barbara Hammer. Interpretable discriminative dimensionality reduction and feature selection on the manifold. In Ulf Brefeld, Elisa Fromont, Andreas Hotho, Arno Knobbe, Marloes Maathuis, and Céline Robardet, editors, *Machine Learning and Knowledge Discovery in Databases*, pages 310–326, Cham, 2020. Springer International Publishing.
- [19] Guillaume Huguet, Alexander Tong, Edward De Brouwer, Yanlei Zhang, Guy Wolf, Ian Adelstein, and Smita Krishnaswamy. A heat diffusion perspective on geodesic preserving dimensionality reduction. In *Thirty-seventh Conference on Neural Information Processing Systems*, 2023.
- [20] Sadamori Kojaku, Jisung Yoon, Isabel Constantino, and Yong-Yeol Ahn. Residual2vec: Debiasing graph embedding with random graphs. In M. Ranzato, A. Beygelzimer, Y. Dauphin, P.S. Liang, and J. Wortman Vaughan, editors, *Advances in Neural Information Processing Systems*, volume 34, pages 24150–24163. Curran Associates, Inc., 2021.
- [21] Leland McInnes, John Healy, and James Melville. Umap: Uniform manifold approximation and projection for dimension reduction, 2018.
- [22] Isaac Z. Pesenson. Sampling in paley-wiener spaces on combinatorial graphs. *Transactions of the American Mathematical Society*, 360:5603–5627, 2008.
- [23] Mauro Maggioni Ronald R. Coifman. Diffusion wavelets. *Applied and Computational Harmonic Analysis*, 2006.

- [24] S. Roweis and L. Saul. Nonlinear dimensionality reduction by locally linear embedding. *SCIENCE*, 290:2323–2326, 2000.
- [25] Atsushi Suzuki, Atsushi Nitanda, jing wang, Linchuan Xu, Kenji Yamanishi, and Marc Cavazza. Generalization bounds for graph embedding using negative sampling: Linear vs hyperbolic. In M. Ranzato, A. Beygelzimer, Y. Dauphin, P.S. Liang, and J. Wortman Vaughan, editors, *Advances in Neural Information Processing Systems*, volume 34, pages 1243–1255. Curran Associates, Inc., 2021.
- [26] Jian Tang, Jingzhou Liu, Ming Zhang, and Qiaozhu Mei. Visualizing large-scale and high-dimensional data. In *Proceedings of the 25th International Conference on World Wide Web*, page 287–297. International World Wide Web Conferences Steering Committee, 2016.
- [27] J. Tenenbaum, V. de Silva, and J. Langford. A global geometric framework for nonlinear dimensionality reduction. *Science*, 2000.
- [28] Laurens van der Maaten and Geoffrey Hinton. Visualizing data using t-SNE. *Journal of Machine Learning Research*, pages 2579–2605, 2008.
- [29] Yongjin Xian, Bernt Schiele, and Zeynep Akata. Zero-shot learning — the good, the bad and the ugly. *2017 IEEE Conference on Computer Vision and Pattern Recognition (CVPR)*, pages 3077–3086, 2017.
- [30] Yuchen Yan, Baoyu Jing, Lihui Liu, Ruijie Wang, Jinning Li, Tarek Abdelzaher, and Hanghang Tong. Reconciling competing sampling strategies of network embedding. In A. Oh, T. Naumann, A. Globerson, K. Saenko, M. Hardt, and S. Levine, editors, *Advances in Neural Information Processing Systems*, volume 36, pages 6844–6861. Curran Associates, Inc., 2023.
- [31] Arman S. Zharmagambetov and Miguel A. Carreira-Perpinan. Learning interpretable, tree-based projection mappings for nonlinear embeddings. In Gustau Camps-Valls, Francisco J. R. Ruiz, and Isabel Valera, editors, *Proceedings of The 25th International Conference on Artificial Intelligence and Statistics*, volume 151 of *Proceedings of Machine Learning Research*, pages 9550–9570. PMLR, 28–30 Mar 2022.
- [32] Rapolas Zilionis, Camilla Engblom, Christina Pfirschke, Virginia Savova, David Zemmour, Hatice Duygu Saatcioglu, Indira Krishnan, Giorgia Maroni, Claire V Meyerovitz, C. Michael Kerwin, Sun Choi, William G Richards, Assunta De Rienzo, Daniel Geoffrey Tenen, Raphael Bueno, Elena Levantini, Mikael J. Pittet, and Allon M. Klein. Single-cell transcriptomics of human and mouse lung cancers reveals conserved myeloid populations across individuals and species. *Immunity*, 2019.

Appendix

9 Dataset Details

Two Moons. The two moons dataset depicts two interleaving half-circles. We sampled $N = 600$ points and used a Gaussian noise level having standard deviation 0.12. An example is show in Figure 3. More specifically, to produce these points we use Sci-kit Learn’s `sklearn.datasets.make_moons` function with $n_samples = 600$ and $noise = 0.12$.

In Figure 3, we show example clusterings for each of the methods mentioned in Section 7.

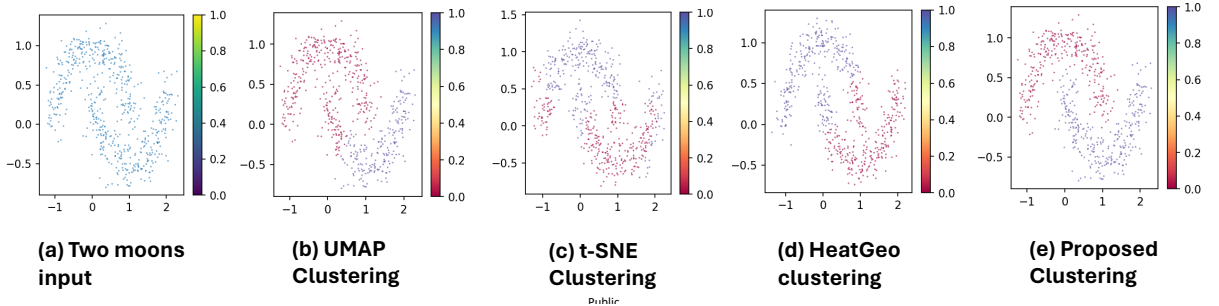


Figure 3: Clustering results using two moons

Census. From the UCI Machine Learning Repository [12], this dataset contains 14 features that are a mix of categorical, numerical, and binary. Such features include age, marital status, sex, etc. The goal is to predict whether a sample makes less than or equal to \$50,000, or strictly more. We use 32,561 samples in our dataset.

Lung Cancer. The Zilionis dataset is widely used, and consists of single-cell RNA sequencing data. It has 306 features, and 48,969 samples. The data has 20 classes corresponding to cell type. More can be found at [32].

Animals with Attributes. The Animals with Attributes (AWA) dataset, contains 5,000 data points corresponding to 10 unseen classes, where the testing image features are obtained from the pre-trained ResNet architecture, with $D = 2,048$ dimensions, and the semantic features are provided with $D = 85$ dimensions. More information can be found in Section 4.1 of [29].

10 Experimental Results on More Datasets

Here we show further experiments on more datasets.

Dense cluster inside a sparse circle: In this example, we sampled 500 points from a dense cluster (using a uniform distribution) situated in the interior of a sparse cluster (using 100 points), maintaining a ratio of 5:1. UMAP relies on a well-initialized kNN graph, however the disparate densities in the two manifolds lead to erroneous edge weights, resulting in errors in segmentation. Despite utilizing the same initial graph construction as UMAP, our method, employing a multi-scale representation, is more successful in segmenting the two manifolds accurately in the presence of differing densities. HeatGeo, a competitive state-of-the-art method, does the best here, and is able to separate the dense-sparse circles from each other.

11 HeatGeo Hyperparameter Tuning Details

We tune HeatGeo on each dataset in Section 7, by tuning over the parameter space:

Data	Dense-sparse clusters	
	ARI	AMI
UMAP	0.75	0.72
t-SNE	0.30	0.33
ISOMAP	0.74	0.65
Diffusion Maps	0.81	0.76
HeatGeo	1.0	1.0
Ms-IMAP Method 1	0.82	0.8
Ms-IMAP Tensor-encoding Method 2	0.77	0.73

Table 3: Comparison of clustering performance on Two Moons and Dense-sparse clusters datasets.

Hyperparameter	Set of values
knn	5, 10, 15
lap_type	normalized, combinatorial
harnack_regul	0, 0.5, 1

Table 4: Space of parameters in which we tuned HeatGeo.

12 Ablation Studies of Hyperparameters for MS-IMAP

Here we study what effect the hyperparameters – the number of nearest neighbors, and the number of filters – have on the clustering performance of MS-IMAP with method 2. In table 5, we demonstrate the effect of varying the number of neighbors, between 10, 15, and 20 neighbors. We see that the results are mostly the same, thus showing MS-IMAP is robust on real datasets.

Dataset	Census		Zilionis		AwA	
	ARI	AMI	ARI	AMI	ARI	AMI
Number of Neighbors / Accuracy						
10	0.22	0.15	0.71	0.78	0.73	0.80
15	0.22	0.15	0.70	0.76	0.74	0.81
20	0.22	0.15	0.70	0.77	0.71	0.79

Table 5: Ablation study on MS-IMAP with method 2, varying the number of neighbors. The number of filters is kept at 5.

We also study the effect of varying the number filters. In table 6, we also see similar results when using different filters, showing the stability of MS-IMAP.

Dataset	Census		Zilionis		AwA	
	ARI	AMI	ARI	AMI	ARI	AMI
5	0.22	0.15	0.70	0.76	0.74	0.81
6	0.22	0.15	0.70	0.76	0.73	0.81
7	0.22	0.15	0.72	0.78	0.74	0.81

Table 6: Ablation study on MS-IMAP with method 2, varying the number of filters. The number of neighbors is kept at 15.

13 Ablation Studies of Hyperparameters for t-SNE, Isomaps, and Diffusion Maps

We study the effect of varying the number of neighbors for the methods: t-SNE, Isomaps, and Diffusion Maps. For t-SNE this would be the perplexity hyperparameter, for Isomaps this would be the number of neighbors, and for diffusion maps, this would be the parameter that affects the width of the Gaussian kernel, i.e. $\exp(\cdot/\alpha)$.

In Table 7, we see choosing a smaller perplexity of 15 does worse than the perplexity of 30 and 60.

Dataset	Census		Zilionis		AwA	
	ARI	AMI	ARI	AMI	ARI	AMI
Perplexity / Accuracy						
15	0.03	0.04	0.37	0.67	0.69	0.76
30	0.15	0.15	0.38	0.68	0.73	0.80
60	0.17	0.17	0.38	0.69	0.73	0.80

Table 7: Ablation study on t-SNE, varying the perplexity.

In Table 8, we see a similar pattern to t-SNE, where choosing too low causes reduction in performance. But performance stabilizes around choosing the number of neighbors as 5-10+.

Dataset	Census		Zilionis		AwA	
	Neighbors / Accuracy	ARI	AMI	ARI	AMI	ARI
2	-0.05	0.02	0.41	0.55	0.43	0.58
5	0.18	0.09	0.44	0.56	0.52	0.60
10	0.18	0.09	0.44	0.57	0.51	0.62

Table 8: Ablation study on Isomap, varying the number of neighbors.

In Table 9, we find the ablation study for Diffusion Maps. Diffusion Maps perform the worst, but as with t-SNE and Isomap, benefits from considering more neighbors.

Dataset	Census		Zilionis		AwA	
	ARI	AMI	ARI	AMI	ARI	AMI
1	0	0	0	0.01	0.23	0.44
2	0	0	0	0.01	0.22	0.43
3	0.06	0.16	0	0.02	0.22	0.42

Table 9: Ablation study on Diffusion Map, varying alpha which affects the width of the kernel.

14 Fast computation using Chebyshev polynomials

We provide additional details regarding the fast computation of SGW coefficients [15]. Directly computing the SGW coefficients above requires calculating the entire eigensystem of the Laplacian, which is computationally intensive - $O(N^3)$ for N points. Instead, Hammond et al. [15] suggested computing the SGW using a fast algorithm based on approximating the scaled generating kernels through low-order polynomials. The wavelet coefficients at each scale are then computed as a polynomial of \mathbf{L} applied to the input data, using approximating polynomials given by truncated Chebyshev polynomials.

The Chebyshev polynomials $T_k(y)$ are computed using the recursive relations: $T_k(y) = 2yT_{k-1}(y) - T_{k-2}(y)$ for $k \geq 2$, where $T_0 = 1$ and $T_1 = y$.

The SGW coefficients are then approximated using wavelet and scaling function coefficients as follows:

$$\psi_f(s_j, i) \sim \left(\frac{1}{2} c_{j,0} f + \sum_{k=1}^K c_{j,k} \bar{T}_{j,k}(\mathbf{L}) f \right)_i \quad (12)$$

where $c_{j,k}, j > 0$ are the Chebyshev coefficients and $\bar{T}_{j,k}$ are the shifted Chebyshev polynomials $\bar{T}_k(x) = T_k\left(\frac{x-a}{a}\right)$ for $x \in [0, \lambda_{\max}]$, where $x = a(y+1)$, $a = \lambda_{\max}$. The scaling function coefficients, which are corresponding to a low-pass filter operation, are approximated in a similar way using Chebyshev polynomials. Note that the scaling kernel function is a low pass filter h satisfying $h(0) > 0$ and $h(x) \rightarrow 0$ when $x \rightarrow \infty$. If the graph is sparse, we obtain a fast computation of the matrix-vector multiplication $\bar{T}_{j,k}(\mathbf{L})f$, where the computational complexity scales linearly with the number of points, resulting in a complexity of $O(N)$ for an input signal $f \in \mathbb{R}^N$. The SGWs efficiently map an input graph signal (a vector of dimension N) to NK scaling and wavelet coefficients.

15 Runtime and Computational Complexity

We have performed experimental runtime studies on empirical datasets. Experiments were performed on Virtual Server containers with 32 cores Intel Xeon 8259CL running at 2.50Ghz and 256GB of RAM. On the AWA dataset of 5,685 samples and 2,048 features, Method 1 and the 3D based Tensor Method 2 both run in 1.35 mins. Finally on the Cancer QC data-set of 48,969 samples and 306 features, Method 1 took 12.44 mins. The computational complexity of Multi-Scale UMAP is of $O(ND\log(N))$ for construction of the multi-scale representations which includes the k nearest neighbor graph using k-d tree, the SGW transform which is $O(N)$ for each dimension of the manifold for sparse graphs. The optimization stage has a complexity which scale with the number of edges in the graph, which has a complexity of $O(kDN)$.

16 Theoretical results: Sampling set for Smooth Manifolds with functions defined over Paley-Wiener Spaces

In this work, we characterize the theoretical properties of the representation power of the SGW operator by considering functions sampled from the Paley-Wiener spaces [22] on combinatorial graphs. The Paley-Wiener spaces were introduced on combinatorial graphs in [22] and a corresponding sampling theory was developed which resembles the classical one. Pesenson proved in [22] that Paley-Wiener functions of low type are uniquely determined by their values on certain subgraphs (which are composed from set of nodes known as the uniqueness sets) and can be reconstructed from such sets in a stable way. We demonstrate that the SGW operator can represent functions f that reside in the Paley-Wiener space on combinatorial graphs more efficiently than the graph Laplacian operator \mathcal{L} . The effectiveness of the SGW operator representation in this case can be understood in several ways. In one way, by the ability of the SGW operator to accurately represent functions with larger bandwidth, i.e., $f \in PW_{\omega'}(G)$ where $\omega < \omega'$.

In order to prove these results, we will first need the following definitions:

Definition 1 *The Paley-Wiener space of ω -bandlimited signals is defined as follows:*

$$PW_{\omega}(G) = \left\{ f \mid \hat{f}(\lambda) = 0 \quad \forall \lambda > \omega \right\} \quad (13)$$

We summarize the main notions and definitions. We consider simple undirected unweighted and connected graph $G = (V, \mathbf{W})$, where V is its set of N vertices and \mathbf{W} is its set of edges. The degree of v is number of vertices adjacent to a vertex v and is denoted by $d(v)$. We assume that degrees of all vertices are bounded by the maximum degree denoted as

$$d(G) = \max_{v \in V} d(v) \quad (14)$$

The following definition [22] explains the uniqueness set.

Definition 2 *A set of vertices $U \subset V$ is a uniqueness set for a space $PW_{\omega}(G)$ if we have two functions from $PW_{\omega}(G)$ that coincide on U then they coincide on V .*

Next the following definition of $L_2(S)$ is provided as the set of finite energy signals whose support is contained in S . The space $L_2(G)$ is the Hilbert space of all complex-valued functions $f : V \rightarrow \mathbb{C}$ with the following inner product $\langle f, g \rangle = \sum_{v \in G} f(v)\overline{g(v)}$ and the norm

$$\|f\| = \left(\sum_{v \in V} |f(v)|^2 \right)^{1/2} \quad (15)$$

The Laplace (normalized) operator \mathcal{L} is defined by the formula [22]:

$$\mathcal{L}f(v) = \frac{1}{\sqrt{d(v)}} \sum_{u \sim v} \left(\frac{f(v)}{\sqrt{d(v)}} - \frac{f(u)}{\sqrt{d(u)}} \right), f \in L_2(G) \quad (16)$$

Definition 3 *For a subset $S \subset V$, denote $L_2(S)$ as the space of all functions from $L_2(G)$ with support in S :*

$$L_2(S) = \{ \varphi \in L_2(G), \varphi(v) = 0, v \in V(G) \setminus S \}$$

Definition 4 [22] We say that a set of vertices $S \subset V$ is a Λ -set if for any $\varphi \in L_2(S)$ it admits a Poincare inequality with a constant $\Lambda(S) > 0$

$$\|\varphi\| \leq \Lambda \|\mathcal{L}\varphi\|, \varphi \in L_2(S) \quad (17)$$

The infimum of all $\Lambda(S) > 0$ for which S is a Λ -set will be called the Poincare constant of the set S and denoted by Λ .

Definition above provides a tool to determine when bandlimited signals in Paley-Wiener spaces $PW_\omega(G)$ can be uniquely represented from their samples on a given set. The role of Λ -sets was explained and proved in the following Theorem by Pesenson [22], that shows that if $S \subset V$ then any signal $f \in PW_\omega(G)$ can be uniquely represented by its samples in the complement set $U = V(G) \setminus S$:

Theorem 2 [22] If $S \subset V$ is a Λ -set, then the set $U = V(G) \setminus S$ is a uniqueness set for any space $PW_\omega(G)$ with $\omega < \frac{1}{\Lambda}$.

Remark: Note that non-trivial uniqueness sets can not exist for functions from any Paley-Wiener subspace $PW_\omega(G)$ with any $\lambda_0 \leq \omega \leq \lambda_N$, but can they can exist for some range $\lambda_0 \leq \omega < \Omega$, as was shown in [22].

We state one of our main results, in which we employ the SGW operator ψ to characterize the uniqueness set using the Λ_ψ -set, therefore extending the Λ -set concerning the graph Laplacian operator \mathcal{L} .

Theorem 3 Let $G = (V, \mathbf{W})$ be a connected graph with N vertices. Assume that there exist a set of vertices $S \subset V$ for which the conditions (1)-(2) in Lemma 1 hold true. Let ψ be the SGW operator using a polynomial $p(\mathcal{L})$ with the coefficients $\{a_k\}_{k=0}^K$ such that $\psi_f = \sum_{k=0}^K a_k \mathcal{L}^k f$. Then, for any $\varphi \in L_2(S)$, we have that the following inequality holds:

$$\|\varphi\| \leq \Lambda_\psi \|\psi_\varphi\| \quad (18)$$

and thus the set S is a Λ_ψ -set for the operator ψ with $\Lambda_\psi = \frac{1}{\sqrt{\sum_{k=0}^K \frac{a_k^2}{\Lambda^{2k}}}}$.

We recall the following results from [22]. Note that [22] established the construction of a Λ -set by imposing specific assumptions on the sets S and U . Our result Theorem 3 holds similar assumptions as in [22].

Lemma 1 [22] Given a connected graph $G = (V, \mathbf{W})$ graph with N vertices for which the following conditions hold true: (1) For every $s \in S$ there exists $u \in U$ that is a neighbor of s , i.e., $w(u, s) > 0$. (2) for every $s \in S$ there exists at least one neighbor node $u \in U$ whose adjacency set intersects S only over s .

Then there exist a set of vertices $S \subset V$ which is a Λ -set, with $\Lambda = d(G)$.

In the next theorem, we expand the characterization of the uniqueness set using the Λ -set concerning the graph Laplacian operator \mathcal{L} to include cases where we employ the SGW operator ψ . We thereby characterize the uniqueness set using the Λ_ψ -set for the SGW operator.

We now turn to prove Theorem 3, which was stated earlier.

Proof of Theorem 3:

Assuming $f \in PW_\omega(G)$, f can be efficiently represented using a polynomial $p(\mathcal{L})$ instead of a kernel

function g , where the wavelet at node i and a fixed scale s is calculated using the polynomial $p(\mathcal{L})$ of the Laplacian:

$$\psi(i) = \sum_{k=0}^K a_k \mathcal{L}^k \delta_i \quad (19)$$

and we can write the SGW coefficients with respect to the function φ as:

$$\psi_\varphi = \sum_{l=0}^{N-1} \sum_{k=0}^K a_k \mathcal{L}^k \varphi$$

Following the assumptions of Theorem 1 implies that there exists a subset $U^* \subset U$ such that for every $s \in S$ there exists at least one point $u^* \in U^*$ whose adjacency set intersects S only over s and from this property we have

$$\mathcal{L}\varphi(u^*) = -\frac{\varphi(s)}{\sqrt{d(s)d(u^*)}}, u^* \in U^*, s \in S \quad (20)$$

We will use this property to show that the set S is a Λ_ψ -set with respect to the operator ψ . Using 20 and taking powers of the Laplacian operator considering $u^* \in U^*, s \in S$ we have that:

$$\mathcal{L}^k \varphi(u^*) = (-1)^k \frac{\varphi(s)}{(d(s)d(u^*))^{k/2}}, u^* \in U^*, s \in S \quad (21)$$

and

$$|\mathcal{L}^k \varphi(u^*)| \geq \frac{|\varphi(s)|}{\Lambda^k}, u^* \in U^*, s \in S \quad (22)$$

Thus we have that $\forall \varphi \in L_2(S)$

$$||\psi_\varphi|| = \left(\sum_{i,j} \sum_{k=0}^K |a_k (\mathcal{L}^k \varphi)_{ij}|^2 \right)^{1/2} \geq \left(\sum_{s \in S} \sum_{k=0}^K |a_k (\mathcal{L}^k \varphi(u^*))|^2 \right)^{1/2} \quad (23)$$

using similar argument as in Lemma 1 we have that

$$\left(\sum_{k=0}^K \sum_{s \in S} |a_k \mathcal{L}^k \varphi(u^*)|^2 \right)^{1/2} = \left(\sum_{k=0}^K |a_k|^2 \sum_{s \in S} |\mathcal{L}^k \varphi(u^*)|^2 \right)^{1/2} \geq ||\varphi|| \left(\sum_{k=0}^K |a_k|^2 \frac{1}{\Lambda^{2k}} \right)^{1/2} \quad (24)$$

which proves the claim of the Theorem. \square

Remark 1: An important property which can be observed from Theorem 3 is the following: given the SGW ψ_f as a spectral representation operator, we can choose coefficients $\{a_k\}_{k=0}^K$ such that we obtain a Λ_ψ - set associated with the operator ψ , which is smaller than the Λ - set associated with the Laplacian operator \mathcal{L} . This implies that the operator ψ provides more flexibility and better control over smoothness properties in comparison to the Laplacian operator.

Remark 2: Since the Λ_ψ - set can be chosen to be smaller than Λ - set (for a proper choice of the coefficients $\{a_k\}_{k=0}^K$ using the operator ψ) then the SGW operator ψ provides a more efficient representation for $f \in PW_{\omega'}(G)$ with $\omega < \omega'$ using the same subsets of nodes from the uniqueness set U in comparison to the Laplacian operator \mathcal{L} .

Remark 3: Note that the characterization of the the uniqueness set does not rely on a reconstruction method of the graph signal values of $f(S)$ from their known values on U .

The next Theorem demonstrates the role of the Λ_ψ -set with respect to the operator ψ , where we show that any signal $f \in PW_\omega(G)$ can be uniquely represented by its samples on the uniqueness set U . This results resembles the role of Λ -sets with respect to the graph Laplacian operator \mathcal{L} , yet with a different bound then Lemma 2.

Theorem 4 *Let $G = (V, \mathbf{W})$ be a connected graph with N vertices and $f \in PW_\omega(G)$ for $\lambda_1 < \omega < \lambda_{\max}$. Given the SGW operator ψ , and a set S which is a Λ_ψ -set. Then the set $U = V \setminus S$ is a uniqueness set for any space $PW_\omega(G)$ with $\omega < 1/\Lambda_\psi$.*

Proof: Given $f, \tilde{f} \in PW_\omega(G)$, then $f - \tilde{f} \in PW_\omega(G)$. Assume that $f \neq \tilde{f}$. If f, \tilde{f} coincide on $U = V \setminus S$, then $f - \tilde{f} \in L_2(S)$ and therefore

$$\|f - \tilde{f}\| \leq \Lambda_\psi \|\psi_{f - \tilde{f}}\| \quad (25)$$

Since $\psi_f \in \mathbb{R}^N$, we have that by properties of a vector space in \mathbb{R}^N , using the Cauchy–Schwarz inequality and assuming $|a_k| \leq 1 \forall k$, we have:

$$\|\psi_{f - \tilde{f}}\| \leq \omega \|f - \tilde{f}\| \quad (26)$$

Combining the inequalities above and using the inequality $\Lambda_\psi \omega < 1$ we have that

$$\|f - \tilde{f}\| \leq \Lambda_\psi \|\psi_{f - \tilde{f}}\| \leq \Lambda_\psi \omega \|f - \tilde{f}\| < \|f - \tilde{f}\| \quad (27)$$

which is a contradiction to the assumption that $f \neq \tilde{f}$. Thus, the set $U = V \setminus S$ is a uniqueness set for any space $PW_\omega(G)$ with $\omega < 1/\Lambda_\psi$. \square

Remark 1: Note that $\Lambda \omega < 1$ implies that $\Lambda_\psi \omega < 1$ given $\Lambda_\psi < \Lambda$, then we can increase the size number of nodes in the uniqueness set U for $PW_\omega(G)$ (for a proper choice of the coefficients $\{a_k\}_{k=0}^K$ using the operator ψ). In other words, we may increase the size of S (thus reducing the size of U) and still obtain a uniqueness set with a smaller size for the graph signals in $PW_\omega(G)$.

Remark 2: We note that the results of Theorem 4 concerning the uniqueness set are independent from the stability properties of the representation. In order to achieve stability which is important for reconstruction, it is required to construct a wavelet operator using multiple scales $t_j, j = 1, \dots, K$, as proposed in [15], which will yield a collection of nK wavelets. More specifically, we can express the function φ using multiple scales t_j (here we replace the previous notation of scale s_j with $t_j, j = 1, \dots, K$, not to confuse with nodes $s \in S$).

Then for a fixed scale t_j we have that the SGW is given by $\|\psi_\varphi(t_j)\| = \left(\sum_{i=1}^N \sum_{k=0}^K |a_{t_j, k}(\mathcal{L}^k \varphi(i))|^2 \right)^{1/2}$ and

$$\|\psi_\varphi\| = \left(\sum_j \sum_{i=1}^N \sum_{k=0}^K |a_{t_j, k}(\mathcal{L}^k \varphi(i))|^2 \right)^{1/2} \quad (28)$$

In a similar way to the arguments provided in Theorem 3 we can choose coefficients $a_{t_j, k}$ associated with the Laplacian polynomial such that the inequality $\|\varphi\| \leq \Lambda_\psi \|\psi_\varphi\|$ is satisfied.

17 Sampling approach from network features

Our approach revolves around the strategic sampling of edges, emphasizing their importance in the overall network structure. We introduce innovative method for this purpose, such as one leveraging edge betweenness centrality (EBC). In these proposed methods, our approach to edge sampling is guided by the assessed significance of edges with respect to the topological structure of the graph. This methodology extends random sampling techniques commonly employed in contemporary graph embedding, which typically rely on information derived solely from sparse graph connectivity, encompassing nodes within a 1-hop distance on the graph. To elaborate on our sampling approach, we extend the definition of the network $G = (V, \mathbf{W})$ to a triplet $G = (V, \mathbf{W}, \gamma)$ such that $\gamma : V \rightarrow (0, 1]$ is some probability distribution over V (or \mathbf{W}) providing the significance of each node/edge. We choose to estimate γ directly from the graph network using kernel density estimation (KDE).

The kernel density estimator of the distribution $\gamma(V)$, is given by

$$\hat{\gamma}(x) = \frac{1}{Nh} \sum_{i \in V} \frac{\mathbf{K}(\bar{v}(i) - x)}{h} \quad (29)$$

Where \bar{v} accumulate statistics measuring the extent of diffusion spread using SGW among nodes, \mathbf{K} is symmetric kernel function (chosen to be a smooth Gaussian symmetric function), $h > 0$ is the smoothing bandwidth that controls the amount of smoothing.

In a similar way, one can also construct a probability measure $\gamma : V \times V \rightarrow (0, 1]$ describing the significant of an edge. In this case, we choose to calculate the distribution from the edge betweenness centrality measurements (EBC), $\{w_{i,j}^{BE} | i, j \in V, i \sim j\}$ (see Eq. 31) where we use kernel density estimation (KDE) to estimate the density distribution. Let $\gamma : V \times V \rightarrow \mathbb{R}^+$ denote the probability distribution over edges in the graph $G = (V, \mathbf{W})$, using the distribution of EBC, (EBC is defined in Eq. 30). We denote the estimated distribution calculated directly from the EBC measurements as $\gamma(\mathbf{W}^{BE})$. Formally, the kernel density estimator of distribution of EBC, $\gamma(\mathbf{W}^{BE})$ is given by

$$\hat{\gamma}(x) = \frac{1}{N(e)h} \sum_{i \sim j} \frac{\mathbf{K}(w_{i,j}^{BE} - x)}{h} \quad (30)$$

Where $N(e)$ is a fixed number of positive edges to be sampled.

The advantage of using KDE is that it is a non-parametric density estimator, which does not require assumption that the underlying density function is from a parametric family. Note that KDE works by estimating the density at each point (node or edge) as a weighted sum of the densities of neighboring points, with the weights given by a kernel function \mathbf{K} . In our experiments, we used the Gaussian kernel for simplicity, but one can use other kernel choices.

17.1 Sample from Network Features using Edge Betweenness Centrality

Motivation: We employ Edge Betweenness Centrality (EBC) based sampling to create a strategy that samples edges from the EBC distribution. This enables us to optimize embeddings by predominantly using edges with low EBC, which are concentrated in dense clusters. In contrast, high-EBC edges typically occur in transitions between clusters and form a sparser set that is less frequently sampled. During optimization with SGD and negative sampling, these high-EBC edges play a crucial role in revealing the global structure of the network and connections between different clusters.

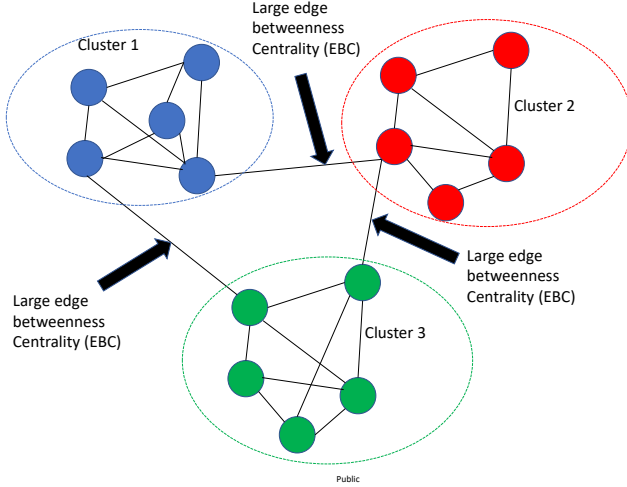


Figure 4: Sampling from Betweenness Centrality distribution

Algorithm 2: Edge Betweenness Centrality Sampling

Input: $G = (V, \mathbf{W})$, kernel density function \mathbf{K} , bandwidth parameter h , N_e for the number of edge samples.

Step 1: Construct the *centrality graph* $G = (V, \mathbf{W}^{BE})$ using Eq. (31).

Step 2: Utilize \mathbf{K} , \bar{v} , and \mathbf{W}^{BE} in Kernel Density Estimation (Eq. 30) to estimate $\hat{\gamma}$.

Step 3: Initialize a list of positive edges $C_e = \{\}$. Set $i = 1$.

Step 4: While $i \leq N_e$ do:

Step 5: Sample an edge w_{ij} using $\hat{\gamma}$, $w_{ij} \sim \hat{\gamma}(\mathbf{W}^{BE})$.

Step 6: Add w_{ij} to C_e , and set $i = i + 1$.

Step 7: Repeat steps 4-6. STOP when $i = N_e$.

Output: Set of edges C_e for positive samples in Algorithm 1.

Consider the illustration in Fig. 4, where edges marked with black arrows correspond to edges with high edge betweenness centrality values, indicating their importance in connecting different dense clusters. Sampling edges with low EBC assists in identifying dominant local structures, while infrequently sampling high betweenness centrality edges is critical for understanding large clusters and the network's global structure.

The Edge Betweenness Centrality:

Edge Betweenness Centrality (EBC) quantifies edge importance based on the fraction of shortest paths that pass through it. For a graph with vertices and edge weights, the EBC of an edge (i, j) is given by:

$$w_{i,j}^{BE} = \sum_{k \neq t} \frac{\sigma_{kt}(w_{ij})}{\sigma_{kt}} \quad (31)$$

Here, σ_{kt} is the number of shortest paths from node k to node t , and $\sigma_{kt}(w_{ij})$ is the number of those paths that include the edge w_{ij} . The centrality graph $G = (V, \mathbf{W}^{BE})$ is constructed using these EBC values, modifying the edges of the original graph G .

Sampling Strategy of EBC using KDE estimator:

Let $\gamma : V \times V \rightarrow \mathbb{R}^+$ denote the probability distribution over edges in the graph $G = (V, \mathbf{W})$, using the distribution of EBC. We denote the estimated distribution calculated directly from the EBC measurements as $\gamma(\mathbf{W}^{\text{BE}})$.

Given the set of edge betweenness centrality $\{w_{i,j}^{\text{BE}} | i, j \in V, i \sim j\}$ as an input to the Kernel Density Estimation (KDE) estimator, the density function is estimated automatically. With a fixed number of positive edges $N(e)$ to be sampled, we sample $N(e)$ edges from the estimated distribution. Although we used the Gaussian kernel in our experiments, other kernel choices are viable. In EBC based-sampling, we sample from the distribution of edge betweenness centrality measurements. This approach prioritizes the sampling of edges based on their importance in the graph structure. By treating edges as bottlenecks, we sample high betweenness centrality edges less frequently, thereby revealing clusters. Edge betweenness centrality serves as a measure of an edge's bottleneck potential, guiding our SGD sampling and prioritizing edges based on their relevance and significance in capturing underlying relationships and connectivity patterns in the graph. Combined with the proposed encoding and initial embedding of multi-scale graph structure, the approach provides a comprehensive representation of the data.